Anisotropic elastic wavefield imaging using the energy norm

Daniel Rocha[1], Nicolay Tanushev[2] & Paul Sava[1]
[1]*Center for Wave Phenomena, Colorado School of Mines*
[2]*Z-Terra, Inc*

ABSTRACT

Based on the energy conservation principle, we derive a scalar imaging condition for anisotropic elastic wavefield migration. Compared to conventional imaging conditions that simply correlate displacement components or potentials from source and receiver wavefields, the proposed imaging condition does not suffer from polarity reversal, which degrades the image quality after stacking over shots. Our imaging condition also accounts for the directionality of the wavefields in space and time, leading to the attenuation of backscattering artifacts, which commonly appear in elastic reverse-time migration images in the presence of strong model contrasts. In addition, our new imaging condition does not require wave-mode decomposition, which demands significant additional cost for elastic wavefields in anisotropic media. To properly image structures, we rely on the anisotropy parameters used in migration, as one would do for any other imaging condition. The application of our imaging condition is suitable for arbitrary anisotropy. We show how the energy imaging condition works by performing numerical experiments and we compare its quality to conventional counterparts by simulating complex geological settings, such as dipping layers characterized by tilted transverse isotropy (TTI).

Key words: anisotropy, imaging condition, conservation of energy, multicomponent, elastic imaging, reverse time migration

1 INTRODUCTION

We frame our paper in the context of (1) an elastic Earth, supporting the propagation of both compressional and shear waves, and (2) an anisotropic Earth, causing wave phenomena such as phase velocity variation with the propagation direction. Although the seismic exploration industry has used the acoustic and isotropic assumptions for a long time, the search for more authentic images and subsurface information, such as fracture distribution, encourages multicomponent elastic wavefield imaging (Denli and Huang, 2008; Yan and Sava, 2011b; Duan and Sava, 2014a; Rocha et al., 2016b). At the same time, data acquired with larger offsets and the increasing number of acquired azimuths enables one to properly account for the influence of anisotropy in order to image complex geological structures (Mikhailov et al., 2001; Lu et al., 2010; Li et al., 2012; McGarry and Qin, 2013; Hu et al., 2014; Wang et al., 2014).

Wavefield imaging, using either the acoustic or elastic wave equation, is implemented in two steps: (1) wavefield extrapolation in the subsurface, using recorded data and an Earth model, and (2) the application of an imaging condition to extract the Earth's reflectivity from the extrapolated wavefields (Claerbout, 1971; Dellinger and Etgen, 1990; Yan and Sava, 2009). If a two-way elastic wave equation is used in the wavefield extrapolation step, followed by the zero-lag crosscorrelation of the wavefields as the imaging condition, the procedure is called elastic reverse time migration (ERTM) (Chang and McMechan, 1987; Hokstad et al., 1998). In recent years, many elastic imaging conditions have been proposed by exploiting the multicomponent aspect of the elastic wavefield and, for the isotropic case, by possibly decomposing the displacement fields into P- and S-wave potentials (Etgen, 1988; Zhe and Greenhalg, 1997; Yan and Sava, 2007; Yan and Xie, 2010; Duan and Sava, 2014a). For anisotropic media, wave-mode decomposition during wavefield extrapolation is feasible but requires additional computational cost and robust techniques (Yan and Sava, 2009, 2011a; Cheng and Fomel, 2013). The correlation of the displacement fields for each component of the source and receiver wavefields is the most common imaging condition for elastic wavefields in anisotropic media. For 3-D imaging, this imaging condition potentially generates nine images with a mixture of wave modes, and this large set of images poses serious difficulties for interpretation.

Another problem exhibited by displacement imaging conditions is polarity reversal, which occurs if one correlates

displacement components from opposite directions. The main disadvantage of polarity reversal is the degradation of image quality after stacking over experiments (Balch and Erdermir, 1994; Yan and Sava, 2008). Similar to wave-mode decomposition, polarity reversal corrections can be implemented with techniques that require additional information about the surbsurface (Duan and Sava, 2014a).

Compared to the acoustic case, elastic imaging involves another issue in addition to polarity reversal. Injection of elastic data into a model (implementing wavefield backpropagation) creates non-physical (or "fake") wave modes during the wavefield extrapolation step, leading to artifacts after the application of an imaging condition (Yan and Sava, 2007; Ravasi and Curtis, 2013; Duan and Sava, 2014a). These artifacts degrade image quality, and might be present even after stacking, masking weak reflections in the final image (Duan and Sava, 2014b). This type of artifacts caused by displacement injection into the model is beyond the scope of this paper.

Analogous to the acoustic case, a second type of artifact appears if the elastic model contains sharp interfaces. In this case, at the wavefield extrapolation step, the sharp interfaces in the Earth model create backscattered reflections, and at the imaging condition step, conventional correlation of the wavefields creates low-wavenumber artifacts in the image (Youn and Zhou, 2001; Yoon and Marfurt, 2006; Guitton et al., 2007; Denli and Huang, 2008; Chen and Huang, 2014; Diaz and Sava, 2015; Rocha et al., 2016b). Ideally, the backscattering artifacts should be attenuated during imaging, without the use of post-imaging artificial filters such as the Laplacian operator (Zhang and Sun, 2009).

Considering these issues, we seek to facilitate interpretation and provide a concise description of the subsurface structures by defining an imaging condition that yields an attribute of the Earth's reflectivity into a single image without wave-mode decomposition, without polarity reversal, and without backscattering artifacts. Our proposed imaging condition is formulated using the energy conservation principle (Yu, 1964; Ben-Menahem and Singh, 1981; Webster, 2000; Rocha et al., 2016a), and extends the previous work on isotropic elastic wavefield imaging (Rocha et al., 2016b).

2 THEORY

We use energy conservation laws analogous to the acoustic and isotropic elastic cases (Rocha et al., 2016a,b) to derive a function that measures the energy of a wavefield in anisotropic media. This energy function also allows us to form an imaging condition for extrapolated elastic wavefields from sources and receivers.

2.1 Elastic wave equation

For an anisotropic medium enclosed by a physical domain $\Omega \subset \mathbb{R}^3$, we can write the equation of motion with no external sources (Aki and Richards, 2002):

$$\rho \ddot{\mathbf{U}} = \nabla \cdot \underline{\mathbf{t}} \,. \tag{1}$$

In equation 1, the displacement field is a function of space ($\mathbf{x}$), time (t), and the experiment index (e): $\mathbf{U}\,(e, \mathbf{x}, t)$ for $\mathbf{x} \in \Omega$ and $t \in [0, T]$, where T is the maximum acquisition time. The experiment index (e) usually represents a shot record, but could also represent a plane wave or other type of shot encoding (Godwin and Sava, 2013). The superscript dot indicates time differentiation. The density is a function of space $\rho(\mathbf{x})$. The underlying bar indicates that the stress is a second-order tensor as a function of space, time and experiment index $\underline{\mathbf{t}}\,(e, \mathbf{x}, t)$. One needs to use certain relations involving material properties to turn equation 1 into a wave equation. Using a general form of linear Hooke's law

$$\underline{\mathbf{t}} = \underline{\underline{\mathbf{c}}}\,\underline{\mathbf{e}} \,, \tag{2}$$

where $\underline{\mathbf{e}}\,(e, \mathbf{x}, t)$ is the strain tensor, $\underline{\underline{\mathbf{c}}}\,(\mathbf{x})$ is the stiffness tensor, and the underlying double bar indicates that the stiffness is a 4th-order tensor. One can rewrite the equation of motion in (1) as a function of the strain tensor

$$\rho \ddot{\mathbf{U}} = \nabla \cdot \left(\underline{\underline{\mathbf{c}}}\,\underline{\mathbf{e}} \right) \,. \tag{3}$$

The strain tensor is a function of the displacement:

$$\underline{\mathbf{e}} = \frac{1}{2} \left(\nabla \mathbf{U} + \nabla \mathbf{U}^{\mathrm{T}} \right) \,. \tag{4}$$

Therefore, using the symmetry of the stiffness tensor, we can rewrite equation 3 as a wave equation:

$$\rho \ddot{\mathbf{U}} = \nabla \cdot \left[\underline{\underline{\mathbf{c}}} \nabla \mathbf{U} \right] \,. \tag{5}$$

Equation 5 can be used to extrapolate elastic wavefield for arbitrary sources, assuming that we know the spatial distribution of the stiffness tensor for a specific type of symmetry.

2.2 Elastic wavefield energy

Analogous to the acoustic and isotropic elastic cases disscussed in Rocha et al. (2016a,b), we develop the energy conservation expression for elastic wavefields in anisotropic media by taking a dot product of the time derivative of the displacement wavefield (i.e., particle velocity) with the corresponding wave equation, followed by integration over the entire physical domain Ω:

$$\int\limits_{\Omega} \rho \dot{\mathbf{U}} \cdot \ddot{\mathbf{U}} d\mathbf{x} = \int\limits_{\Omega} \dot{\mathbf{U}} \cdot \left[\nabla \cdot \left(\underline{\underline{\mathbf{c}}} \nabla \mathbf{U} \right) \right] d\mathbf{x} \,. \tag{6}$$

Rearranging the term on the left-hand side by the chain rule leads to

$$\frac{1}{2} \frac{\partial}{\partial t} \int\limits_{\Omega} \rho \|\dot{\mathbf{U}}\|^2 d\mathbf{x} = \int\limits_{\Omega} \dot{\mathbf{U}} \cdot \left[\nabla \cdot \left(\underline{\underline{\mathbf{c}}} \nabla \mathbf{U} \right) \right] d\mathbf{x} \,. \tag{7}$$

Using the chain rule again on the right-hand side leads to

$$\begin{aligned} \frac{1}{2} \frac{\partial}{\partial t} \int\limits_{\Omega} \rho |\dot{\mathbf{U}}|^2 d\mathbf{x} \quad &= \quad \int\limits_{\Omega} \nabla \cdot \left[\left(\underline{\underline{\mathbf{c}}} \nabla \mathbf{U} \right) \dot{\mathbf{U}} \right] d\mathbf{x} \\ &- \quad \int\limits_{\Omega} \nabla \dot{\mathbf{U}} : \left(\underline{\underline{\mathbf{c}}} \nabla \mathbf{U} \right) d\mathbf{x} \,. \end{aligned} \tag{8}$$

The first term on the right-hand side turns into a surface integral over the boundary using the Divergence Theorem (Boas, 2006). Because we assume homogeneous boundary conditions for the wavefield and its derivatives, this surface integral goes to zero:

$$\frac{1}{2}\frac{\partial}{\partial t}\int\limits_{\Omega}\rho\|\dot{\mathbf{U}}\|^2 d\mathbf{x} = -\int\limits_{\Omega}\nabla\dot{\mathbf{U}} : \left(\underline{\underline{\mathbf{c}}}\nabla\mathbf{U}\right) d\mathbf{x}\ . \tag{9}$$

Developing the remaining term on the right-hand side by using the properties of the Frobenius product (Appendix A), we obtain

$$\int\limits_{\Omega}\nabla\dot{\mathbf{U}} : \left(\underline{\underline{\mathbf{c}}}\nabla\mathbf{U}\right) d\mathbf{x} = \int\limits_{\Omega}\mathrm{Tr}\left[\nabla\dot{\mathbf{U}}^{\mathrm{T}}\left(\underline{\underline{\mathbf{c}}}\nabla\mathbf{U}\right)\right] d\mathbf{x}\ , \tag{10}$$

$$= \frac{1}{2}\frac{\partial}{\partial t}\int\limits_{\Omega}\mathrm{Tr}\left[\nabla\mathbf{U}^{\mathrm{T}}\left(\underline{\underline{\mathbf{c}}}\nabla\mathbf{U}\right)\right] d\mathbf{x}\ , \tag{11}$$

$$= \frac{1}{2}\frac{\partial}{\partial t}\int\limits_{\Omega}\left(\underline{\underline{\mathbf{c}}}\nabla\mathbf{U}\right) : \nabla\mathbf{U}\ d\mathbf{x}\ , \tag{12}$$

where $\mathrm{Tr}(\cdot)$ evaluates the trace of a matrix. Substituting equation 12 in equation 9, we have

$$\frac{1}{2}\frac{\partial}{\partial t}\int\limits_{\Omega}\rho\|\dot{\mathbf{U}}\|^2 + \left(\underline{\underline{\mathbf{c}}}\nabla\mathbf{U}\right) : \nabla\mathbf{U}\ d\mathbf{x} = 0\ . \tag{13}$$

Therefore, the function

$$E(t) = \frac{1}{2}\int\limits_{\Omega}\rho\|\dot{\mathbf{U}}\|^2 + \left(\underline{\underline{\mathbf{c}}}\nabla\mathbf{U}\right) : \nabla\mathbf{U}\ d\mathbf{x} \tag{14}$$

is conserved in time.

2.3 Physical Interpretation

The first term in the integrand of equation 14 represents the kinetic energy of the wavefield, and the second term is the strain energy (Slawinski, 2003), which represents the potential energy of the wavefield. Therefore, equation 13 states the familiar fact that the total energy $E(t)$ is conserved in time. Substituting the stiffness coefficients for the isotropic case in equation 14, we obtain the energy function for the isotropic case shown in Rocha et al. (2016b) (Appendix B):

$$\begin{aligned} E(t) \quad &= \quad \frac{1}{2}\int\limits_{\Omega}\left[\rho\|\dot{\mathbf{U}}\|^2 + \lambda\|\nabla\cdot\mathbf{U}\|^2\right. \\ &+ \quad \left.\mu\left(\nabla\mathbf{U} : \nabla\mathbf{U} + \nabla\mathbf{U} : \nabla\mathbf{U}^{\mathrm{T}}\right)\right] d\mathbf{x}\ . \end{aligned} \tag{15}$$

The individual terms in equations 14 and 15 are also related to nonlinear inversion theory as shown by other authors (Hokstad et al., 1998; Zhu et al., 2009).

2.4 Imaging condition

Considering two wavefields $\mathbf{U}$ and $\mathbf{V}$, and the elastic energy norm in equation 14, we can define the following inner product:

$$< \mathbf{U}, \mathbf{V} >_E = \int\limits_0^T\int\limits_{\Omega}\rho\dot{\mathbf{U}}\cdot\dot{\mathbf{V}} + \left(\underline{\underline{\mathbf{c}}}\nabla\mathbf{U}\right) : \nabla\mathbf{V}\ d\mathbf{x}\ . \tag{16}$$

We propose a new elastic imaging condition based on the inner product in equation 16 between source and receiver wavefields, followed by summation over time and experiments:

$$I_E = \sum_{e,t}\left[\rho\dot{\mathbf{U}}\cdot\dot{\mathbf{V}} + \left(\underline{\underline{\mathbf{c}}}\nabla\mathbf{U}\right) : \nabla\mathbf{V}\right]\ . \tag{17}$$

Here, $\mathbf{U}\,(e,\mathbf{x},t)$ and $\mathbf{V}\,(e,\mathbf{x},t)$ are the source and receiver vector wavefields, respectively, and $I_E\,(\mathbf{x})$ is a scalar image obtained from the elastic wavefields. We can describe this imaging condition as a dot product between the following vectors:

$$\square\mathbf{U} = \left\{\rho^{1/2}\dot{\mathbf{U}}, \underline{\underline{\mathbf{c}}}^{1/2}(\nabla\mathbf{U})\right\}\ , \tag{18}$$

$$\square\mathbf{V} = \left\{\rho^{1/2}\dot{\mathbf{V}}, \underline{\underline{\mathbf{c}}}^{1/2}(\nabla\mathbf{V})\right\}\ . \tag{19}$$

The tensor $\underline{\underline{\mathbf{c}}}^{1/2}$ is the square root of $\underline{\underline{\mathbf{c}}}$, which exists and is unique because $\underline{\underline{\mathbf{c}}}$ is positive definite (Shao and Lu, 2009). Equations 18 and 19 define multidimensional vectors with twelve components (in contrast with three-component vectors in 3-D space). The first three components of the vectors in equations 18 and 19 are proportional to the wavefield time derivatives, $\dot{\mathbf{U}}$ and $\dot{\mathbf{V}}$, and the other nine components are derived from the displacement gradients $\nabla\mathbf{U}$ and $\nabla\mathbf{V}$. We can call $\square\mathbf{U}$ and $\square\mathbf{V}$ "energy" vectors since their norms is equal to the energy norm in equation 14 for a fixed point in space.

Therefore, we can rewrite equation 17 as

$$I_E = \sum_{e,t}\square\mathbf{U}\cdot\square\mathbf{V}\ . \tag{20}$$

This expression is analogous to the similar imaging condition developed for acoustic and isotropic elastic wavefields (Rocha et al., 2016a,b), and has similar physical interpretation and application, as discussed in the next section.

2.5 Backscattering attenuation

Vectors $\square\mathbf{U}$ and $\square\mathbf{V}$ are related to the polarization and propagation direction of the elastic wavefields $\mathbf{U}$ and $\mathbf{V}$. Consider a plane wavefield $\mathbf{U}$ given by

$$\mathbf{U} = \mathbf{u}_0\cos\left[\omega\left(\mathbf{p}\cdot\mathbf{x} - t\right)\right]\ , \tag{21}$$

where $\mathbf{u}_0$ is the polarization vector, $\mathbf{p}$ is the slowness vector, and ω is the frequency. We assume that ω is large compared to the size of the medium and that the vectors $\mathbf{u}_0$ and $\mathbf{p}$ are slowly varying in space and time, which makes the spatial and temporal derivatives of $\mathbf{u}_0$ and $\mathbf{p}$ small compared to ω. We can rewrite equation 21 in index form as

$$U_i = u_i\cos\left[\omega\left(p_m x_m - t\right)\right]\ , \tag{22}$$

where indices $i, m = \{1, 2, 3\}$ represent the Cartesian components of wavefield $\mathbf{U}$. We follow the Einstein convention and all repeated indices are summed over. Substituting the plane wave definition in equation 22 as a trial solution of the elastic equation in 5, and collecting the highest order term in ω, we have

$$\omega^2 \sin\left[\omega\left(p_m x_m - t\right)\right]\left[\rho u_i - u_k c_{ijkl} p_j p_l\right] = 0 \ , \qquad (23)$$

where $j, k, l = \{1, 2, 3\}$. Since equation 23 must hold for any ω, we obtain the Christoffel equation:

$$\rho u_i = u_k c_{ijkl} p_j p_l \ . \qquad (24)$$

The dot product between equation 24 and the polarization vector $\mathbf{u}_0$ yields

$$\rho u_i u_i - u_i u_k c_{ijkl} p_j p_l = 0 \ . \qquad (25)$$

Using equation 22, the term $\dot{\mathbf{U}}$ in index form is

$$\dot{U}_i = \omega u_i \sin\left[\omega\left(p_m x_m - t\right)\right] \ , \qquad (26)$$

and $\nabla\mathbf{U}$ in index form is

$$U_{i,j} = -\omega u_i p_j \sin\left[\omega\left(p_m x_m - t\right)\right] \ , \qquad (27)$$

where subscript indices after the comma symbol indicate spatial derivation with respect to one Cartesian component. Therefore, we can rewrite the norm of $\Box\mathbf{U}$, defined in equation 18, in index form as

$$\|\Box\mathbf{U}\|^2 = \rho \dot{U}_i \dot{U}_i + c_{ijkl} U_{i,j} U_{k,l} \ . \qquad (28)$$

Using equations 26 and 27, the individual terms in equation 28 are

$$\rho \dot{U}_i \dot{U}_i \ = \ \rho \omega^2 u_i u_i \sin^2\left[\omega\left(p_m x_m - t\right)\right] \ , \qquad (29)$$

$$c_{ijkl} U_{i,j} U_{k,l} \ = \ \omega^2 u_i u_k c_{ijkl} p_j p_l \sin^2\left[\omega\left(p_m x_m - t\right)\right] \ . \qquad (30)$$

Hence, the norm of $\Box\mathbf{U}$ is

$$\|\Box\mathbf{U}\|^2 = \omega^2 \Big[\rho u_i u_i + u_i u_k c_{ijkl} p_j p_l\Big] \sin^2\left[\omega\left(p_m x_m - t\right)\right] \ . \qquad (31)$$

We seek to define an imaging condition that attenuates the correlation between waves from the source and receiver wavefields propagating along the same path and with the same polarization, i.e., elastic backscattering. Therefore, elastic backscattering events are characterized by the same plane waves: $V_i = U_i = u_i \cos\left[\omega\left(p_m x_m - t\right)\right]$. Defining $(\Box\mathbf{V})^\dagger$ as

$$(\Box\mathbf{V})^\dagger = \left\{-\rho^{1/2}\mathbf{V}_t, \underline{\underline{\mathbf{c}}}^{1/2}(\nabla\mathbf{V})\right\} \ , \qquad (32)$$

we compute the dot product between $\Box\mathbf{U}$ and $(\Box\mathbf{V})^\dagger$ for backscattering events as

$$\Box\mathbf{U} \cdot (\Box\mathbf{V})^\dagger = \omega^2 [\rho u_i u_i - u_i u_k c_{ijkl} p_j p_l] \sin^2[\omega(p_m x_m - t)]. \qquad (33)$$

Using the relation in equation 25, we obtain

$$\Box\mathbf{U} \cdot (\Box\mathbf{V})^\dagger = 0 \ , \qquad (34)$$

i.e., the dot product is equal to zero everywhere except at the locations where reflectors exist or different wave modes interact, since the vectors $\mathbf{p}$ and $\mathbf{u}_0$ are different for $\mathbf{U}$ and $\mathbf{V}$ at these locations. Therefore, the dot product in equation 34 nullifies the events that propagate along the same path and have the same polarization. Such events include reflection backscattering, diving, direct, and head waves from the same wave modes. Therefore, the imaging condition

$$I_E^\dagger = \sum_{e,t} \Box\mathbf{U} \cdot (\Box\mathbf{V})^\dagger \qquad (35)$$

attenuates backscattering artifacts in elastic RTM images.

3 EXAMPLES

Using a simple model with a horizontal reflector at $z = 1.5$ km and a vertical displacement source function (Figure 1), we test the proposed imaging condition and compare it with the conventional imaging conditions (Figure 2). We refer to the zero-lag correlation between displacement field components as conventional imaging conditions (Yan and Sava, 2007). Figure 1 also shows the model parameters that we use in this experiment following the convention from Thomsen (1986). The presence of the reflector in the migration velocity leads to a velocity contrast, causing backscattering artifacts in the conventional images (Figures 2(a)-2(c)). In addition, the polarity reversal at normal incidence occurs when different components of the displacement field are correlated (Figure 2(b)). In contrast, the energy imaging condition from equation 35 effectively attenuates the backscattering artifacts and shows no polarity reversal at the imaged reflector (Figure 2(d)). Figure 2(d) only contains artifacts that are caused by the non-physical ("fake") modes generated during the wavefield extrapolation. These artifacts are characterized by the correlation of events with different polarization and/or propagation direction. Based on equation 33, the energy image outputs a non-zero dot product between the energy vectors $\Box\mathbf{U}$ and $(\Box\mathbf{V})^\dagger$ for these artifacts. For a multiple-shot experiment, the "fake" modes artifacts are attenuated after stacking over shots, whereas backscattering artifacts and polarity reversal effects are not.

Figures 3-6 show the Marmousi II (Martin et al., 2002) acquisition geometry, model parameters used to simulate synthetic data, the migration model parameters, and the resulted images. As seen in Figure 3, the synthetic data are obtained from a horizontal line of receivers that record the displacement field at every grid point of the water bottom ($z = 0.5$ km), and from 76 pressure sources located near the surface of the water layer ($z = 0.05$ km) with a horizontal spacing of 150 m. This acquisition geometry resembles a multicomponent ocean bottom seismic survey (OBS). The migration model parameters are smoothed versions of the true model parameters (Figures 4 and 5) and contain sufficient sharp interfaces that create backscattering reflections during the wavefield extrapolation. Such interfaces generate artifacts when using conventional imaging conditions. As expected, all conventional images in Figures 6(a)-6(c) contain backscattering artifacts, and Figure 6(b) also shows the effects of a non-constructive stack due to polarity reversal artifacts. In contrast, we attenuate all of

these artifacts in Figure 6(d) using the imaging condition from equation 35. Similar to the simple experiment in Figure 2(d), using our new imaging condition, the individual elastic images for shots have only "fake" mode artifacts, which are attenuated after stacking over shots, thus leading to a good quality image, as seen in Figure 6(d).

Figures 7 and 8 show a 3D elastic experiment with constant model parameters above a horizontal reflector at $z = 0.21$ km. The model consists of a 3D TTI anisotropy symmetry system, and the tilt is determined by a 30° angle with the vertical axis, and an azimuth of 45° with respect to the $x-$axis. We use a vertical dislocation source at the center of the surface ($x = y = 0.45$ km and $z = 0$ km) to generate the source wavefield. The receiver wavefield is extrapolated from receivers at every grid point from the surface ($z = 0$ km). The correlation between displacement components from the source and receiver wavefields generate images with strong backscattering artifacts and polarity reversal effects (Figures 8(a)-Figures 8(c)). Using the energy imaging in equation 35, we form an image with attenuated artifacts and no polarity reversal (Figure 8(d)).

4 CONCLUSIONS

The anisotropic energy imaging condition is applicable for arbitrary anisotropy, produces a scalar image without the need for wave-mode decomposition, and does not suffer from polarity reversal, as is the case for displacement images using different components of the source and receiver wavefields. We describe this imaging condition as the scalar product between the energy vectors $\Box\mathbf{U}$ and $\Box\mathbf{V}$, which are built using the extrapolated wavefields $\mathbf{U}$ and $\mathbf{V}$. As inferred from the definition of these vectors, the proposed imaging condition accounts for wavefield directionality, incorporating the wavefield propagation and polarization directions. By exploiting this directionality, we are able to attenuate the backscattering artifacts in the imaging process, and obtain robust, inexpensive and high-quality elastic images.

5 ACKNOWLEDGMENTS

We would like to thank sponsor companies of the Center for Wave Phenomena, whose support made this research possible. The reproducible numeric examples in this paper use the Madagascar open-source software package (Fomel et al., 2013) freely available from http://www.ahay.org.

REFERENCES

Aki, K., and P. G. Richards, 2002, Quantitative seismology, 2nd ed.: University Science Books.

Balch, A. H., and C. Erdermir, 1994, Sign-change correction for prestack migration of P-S converted wave reflections: Geophysical Prospecting, **42**, 637–663.

Ben-Menahem, A., and S. J. Singh, 1981, Seismic waves and sources, 1st ed.: Springer-Verlag.

Boas, M. L., 2006, Mathematical Methods in the Physical Sciences, 3 ed.: John Wiley & Sons.

Chang, W.-F., and G. A. McMechan, 1987, Elastic reverse-time migration: Geophysics, **52**, 1365–1375.

Chen, T., and L. Huang, 2014, Elastic reverse-time migration with an excitation amplitude imaging condition: Presented at the SEG Denver 2014 Annual Meeting.

Cheng, J., and S. Fomel, 2013, Fast algorithms for elastic-wave-mode separation and vector decomposition using low-rank approximation for anisotropic media: Presented at the SEG Houston 2013 Annual Meeting.

Claerbout, J. F., 1971, Toward a unified theory of reflector mapping: Geophysics, **36**, 467–481.

Dellinger, J., and J. Etgen, 1990, Wave-field separation in two-dimensional anisotropic media: Geophysics, **55**, 914–919.

Denli, H., and L. Huang, 2008, Elastic-wave reverse-time migration with a wavefield-separation imaging condition: Presented at the SEG 2008 Annual Meeting.

Diaz, E., and P. Sava, 2015, Wavefield tomography using reverse time migration backscattering: Geophysics, **80**, R57–R69.

Duan, Y., and P. Sava, 2014a, Converted-waves imaging condition for elastic reverse-time migration: Presented at the SEG 2014 Denver Annual Meeting.

———, 2014b, Elastic reverse-time migration with OBS multiples: Presented at the SEG 2014 Denver Annual Meeting.

Etgen, J. T., 1988, Prestacked migration of P- and SV-waves: Presented at the SEG 1988 Annual Meeting.

Fomel, S., P. Sava, I. Vlad, Y. Liu, and V. Bashkardin, 2013, Madagascar: open-source software project for multidimensional data analysis and reproducible computational experiments: Journal of Open Research Software, **1**.

Godwin, J., and P. Sava, 2013, A comparison of shot-encoding schemes for wave-equation migration: Geophysical Prospecting, **61**, 391–408.

Golub, G. H., and C. F. V. Loan, 1996, Chapter 2 - Matrix Analysis, *in* Matrix computations, 3 ed.: John Hopkins University Press.

Guitton, A., B. Kaelin, and B. Biondi, 2007, Least-squares attenuation of reverse-time-migration artifacts: Geophysics, **72**, S19–S23.

Hokstad, K., R. Mittet, and M. Landrø, 1998, Elastic reverse time migration of marine walkaway vertical seismic profiling data: Geophysics, **63**, 1685–1695.

Hu, C., U. Albertin, and T. Johnsen, 2014, Optical flow equation based imaging condition for elastic reverse time migration: Presented at the SEG 2014 Denver Annual Meeting.

Li, Y., P. Shen, and C. Perkins, 2012, VTI migration velocity analysis using RTM: Presented at the SEG Las Vegas 2012 Annual Meeting.

Lu, R., P. Traynin, T. Dickens, and J. Anderson, 2010, Impact of TTI Anisotropy on Elastic Reverse Time Migration: Presented at the 72nd EAGE Annual Meeting.

Martin, G., K. Marfurt, and S. Larsen, 2002, Marmousi-2,

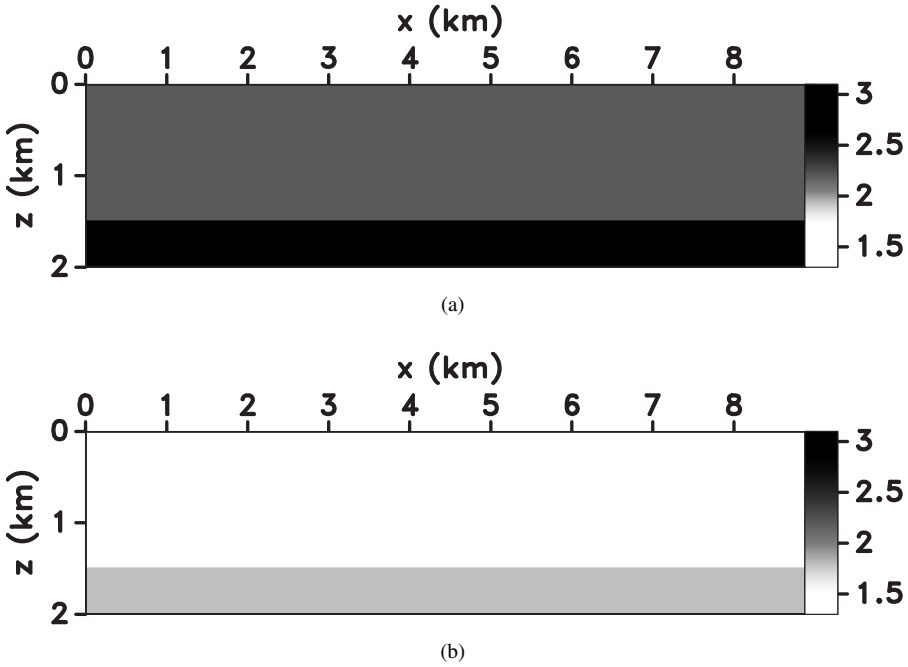

Figure 1. Model parameters used for the experiments in Figure 2: (a) P and (b) S velocity along the symmetry axis. The anisotropy parameters $\epsilon = 0.4$, $\delta = 0.3$ and $\nu = 26^\circ$ are constant for the entire model.

an updated model for the investigation of avo in structurally complex areas: Presented at the 2002 SEG Annual Meeting.

McGarry, R., and Y. Qin, 2013, Direction-vector-based angle gathers from anisotropic elastic RTM: Presented at the SEG 2013 Houston Annual Meeting.

Mikhailov, O., J. Johnson, E. Shoshitaishvili, and C. Frasier, 2001, Practical approach to joint imaging of multicomponent data: The Leading Edge, **20**, 1016–1021.

Ravasi, M., and A. Curtis, 2013, Elastic imaging with exact wavefield extrapolation for application to ocean-bottom 4C seismic data: Geophysics, **78**, S265–S284.

Robert, A., 2005, Linear algebra: Examples and applications: World Scientific, **1**.

Rocha, D., N. Tanushev, and P. Sava, 2016a, Acoustic wavefield imaging using the energy norm: Geophysics (accepted for publication).

———, 2016b, Elastic wavefield imaging using the energy norm: Geophysics (accepted for publication).

Shao, Y., and C. Lu, 2009, A direct proof of uniqueness of square-root of a positive semi-definite tensor: Applied Mathematics and Mechanics, **30**, 713–716.

Slawinski, M. A., 2003, Seismic waves and rays in elastic media, 1st ed.: Elsevier Science, **34**.

Thomsen, L., 1986, Weak elastic anisotropy: Geophysics, **51**, 1954?1966.

Wang, C., J. Cheng, and T. Wang, 2014, Local angle domain elastic reverse time migration in anisotropic media: Presented at the CPS/SEG Beijing 2014 International Geophysical Conference.

Webster, J., 2000, Chapter 8.1 - The Wave Equation, *in* Mechanical variables measurement: solid, fluid and thermal, 1 ed.: CRC Press.

Yan, J., and P. Sava, 2007, Elastic wavefield imaging with scalar and vector potentials: Presented at the SEG Denver 2007 Annual Meeting.

———, 2008, Isotropic angle-domain elastic reverse-time migration: Geophysics, **73**, S229–S239.

———, 2009, Elastic wave-mode separation for VTI media: Geophysics, **74**, WB19–WB32.

———, 2011a, Elastic wave-mode separation for tilted transverse isotropy media: Geophysical Prospecting, **60**, 29–48.

———, 2011b, Improving the efficiency of elastic wave-mode separation for heterogeneous tti media: Geophysics, **76**, T65–T78.

Yan, R., and X.-B. Xie, 2010, The new angle-domain imaging condition for elastic RTM: Presented at the SEG Denver 2010 Annual Meeting.

Yoon, K., and K. J. Marfurt, 2006, Reverse-time migration using the Poynting vector: Exploration Geophysics, **37**, 102–107.

Youn, O., and H. W. Zhou, 2001, Depth imaging with multiples: Geophysics, **66**, 246–255.

Yu, Y.-Y., 1964, Generalized Hamilton's Principle and Variational Equation of Motion in Nonlinear Elasticity Theory, with Application to Plate Theory: The Journal of the Acoustic Society of America, **36**, 111–120.

Zhang, Y., and J. Sun, 2009, Practical issues in reverse time migration: true amplitude gathers, noise removal and harmonic source enconding: First Break, **27**, 53–59.

Zhe, J., and S. A. Greenhalg, 1997, Prestack multicomponent

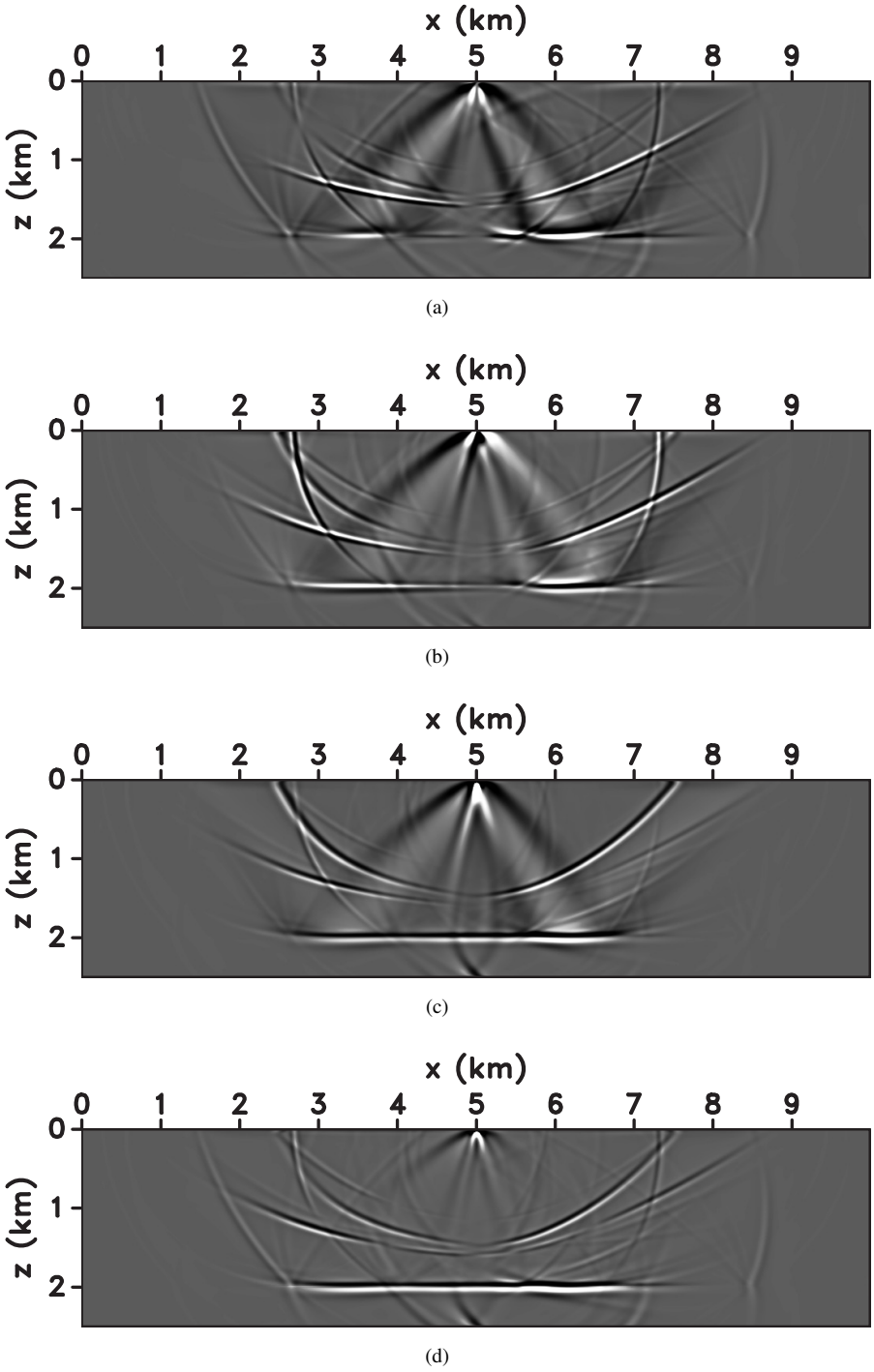

Figure 2. Imaging conditions using displacement components for a horizontal reflector with a vertical displacement source at $x = 5$ km: (a) $U_x V_x$, (b) $U_z V_x$, and (c) $U_z V_z$ image, where $\{U_x, U_z\}$ and $\{V_x, V_z\}$ are the horizontal and vertical components of the source and receiver wavefields, respectively. Artifacts present in all images occur due to the "fake" modes (caused by injection of vector fields). Polarity reversal at normal incidence occurs for the image in (b), and backscattering artifacts occur for images in (a)-(c). Comparing to the other images, the energy image in (d) is the only one with attenuated backscattering artifacts and without polarity reversal at normal incidence.

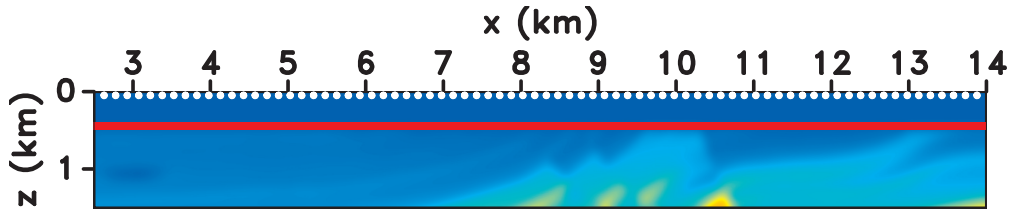

Figure 3. Acquisition geometry used in the Marmousi II experiment. The white dots indicate the positions of the seventy-six pressure sources ($z = 0.05$ km), and the line at the water bottom indicates multicomponent receivers that record the displacement field ($z = 0.5$ km).

migration: Geophysics, **62**, 598–613.

Zhu, H., Y. Luo, T. Nissen-Meyer], C. Morency, and J. Tromp, 2009, Elastic imaging and time-lapse migration based on adjoint methods: Geophysics, **74**, WCA167–WCA177.

Appendix A

Frobenius product and norm

The Frobenius norm in linear algebra generalizes the more conventional vector norm concept. Consider an arbitrary matrix $A_{M\times N}$, this norm is defined as (Golub and Loan, 1996)

$$||A||_F = \sqrt{\sum_{i=1}^{M}\sum_{j=1}^{N}|a_{ij}|^2}\ . \tag{A.1}$$

One can also define a norm of a tensor field using the inner product of associate matrices. Given tensor fields A and B, the Frobenius product is defined as

$$< A, B >_F = A : B = \sum_{i=1}^{M}\sum_{j=1}^{N} a_{ij}b_{ij}\ , \tag{A.2}$$

where M and N are the dimensions of the tensors A and B. This product can also be written in matrix form as

$$< A, B >_F = A : B = \mathrm{Tr}(A^{\mathrm{T}}B) = \mathrm{Tr}(AB^{\mathrm{T}})\ . \tag{A.3}$$

Then, the Frobenius norm of a tensor A is written as

$$||A||_F = \sqrt{\mathrm{Tr}(AA^{\mathrm{T}})}\ . \tag{A.4}$$

Appendix B

Strain-energy function in isotropic media

In a general elastic medium subject to infinitesimal strains, the strain-energy function is (Slawinski, 2003)

$$E(\epsilon) = \frac{1}{2}c_{ijlk}\epsilon_{kl}\epsilon_{ij}\ , \tag{B.1}$$

where c_{ijlk} is an element of the stiffness tensor $\underline{\underline{\mathbf{c}}}$, and ϵ_{ij} is an element of the strain tensor $\underline{\underline{\mathbf{e}}}$. The repeated indices i, j, k, l imply summation, following the Einstein convention (Robert, 2005). For an isotropic medium, the stiffness coefficients are (Aki and Richards, 2002)

$$c_{ijlk} = \lambda\delta_{ij}\delta_{kl} + \mu\delta_{ik}\delta_{jl} + \mu\delta_{il}\delta_{jk}\ , \tag{B.2}$$

where δ_{ij} is the Kronecker delta function, and λ and μ are the Lamé parameters. Substituting equation B.2 in equation B.1, we obtain

$$E(\epsilon) = \frac{1}{2}\left[\lambda\delta_{ij}\delta_{kl} + \mu\delta_{ik}\delta_{jl} + \mu\delta_{il}\delta_{jk}\right]\epsilon_{kl}\epsilon_{ij}\ . \tag{B.3}$$

Considering the Kronecker delta function is equal to unity for equal indices and zero otherwise, we develop each term and obtain

$$E(\epsilon) = \frac{1}{2}\left[\lambda\epsilon_{ii}\epsilon_{kk} + \mu\epsilon_{ij}\epsilon_{ij} + \mu\epsilon_{ji}\epsilon_{ij}\right]. \tag{B.4}$$

These implicit summations can be written in matrix form as

$$E(\mathbf{e}) = \frac{1}{2}\left[\lambda\mathrm{Tr}[\mathbf{e}]\mathrm{Tr}[\mathbf{e}] + \mu\left(\mathbf{e} : \mathbf{e}\right) + \mu\left(\mathbf{e} : \mathbf{e}^{\mathrm{T}}\right)\right]. \tag{B.5}$$

As the strain tensor is symmetric, we obtain

$$E(\mathbf{e}) = \frac{1}{2}\left[\lambda\left(\mathrm{Tr}[\mathbf{e}]\right)^2 + 2\mu\left(\mathbf{e} : \mathbf{e}\right)\right]. \tag{B.6}$$

The strain tensor $\mathbf{e}$ is a function of the wavefield derivatives:

$$\mathbf{e} = \frac{1}{2}\left[\nabla\mathbf{U} + \nabla\mathbf{U}^{\mathrm{T}}\right] \tag{B.7}$$

Substituting equation B.7 in B.6, we obtain

$$\begin{aligned} E(\mathbf{e}) &= \frac{1}{2}\left[\lambda\|\nabla\cdot\mathbf{U}\|^2 + 2\mu\left(\frac{1}{2}\left(\nabla\mathbf{U}+\nabla\mathbf{U}^{\mathrm{T}}\right) : \frac{1}{2}\left(\nabla\mathbf{U}+\nabla\mathbf{U}^{\mathrm{T}}\right)\right)\right] \\ &= \frac{1}{2}\left[\lambda\|\nabla\cdot\mathbf{U}\|^2 + \frac{\mu}{2}\left(\nabla\mathbf{U}:\nabla\mathbf{U} + 2\nabla\mathbf{U}:\nabla\mathbf{U}^{\mathrm{T}} + \nabla\mathbf{U}^{\mathrm{T}}:\nabla\mathbf{U}^{\mathrm{T}}\right)\right] \\ &= \frac{1}{2}\left[\lambda\|\nabla\cdot\mathbf{U}\|^2 + \mu\left(\nabla\mathbf{U}:\nabla\mathbf{U} + \nabla\mathbf{U}:\nabla\mathbf{U}^{\mathrm{T}}\right)\right]\ , \end{aligned} \tag{B.8}$$

which corresponds to the potential energy terms of equation 15.

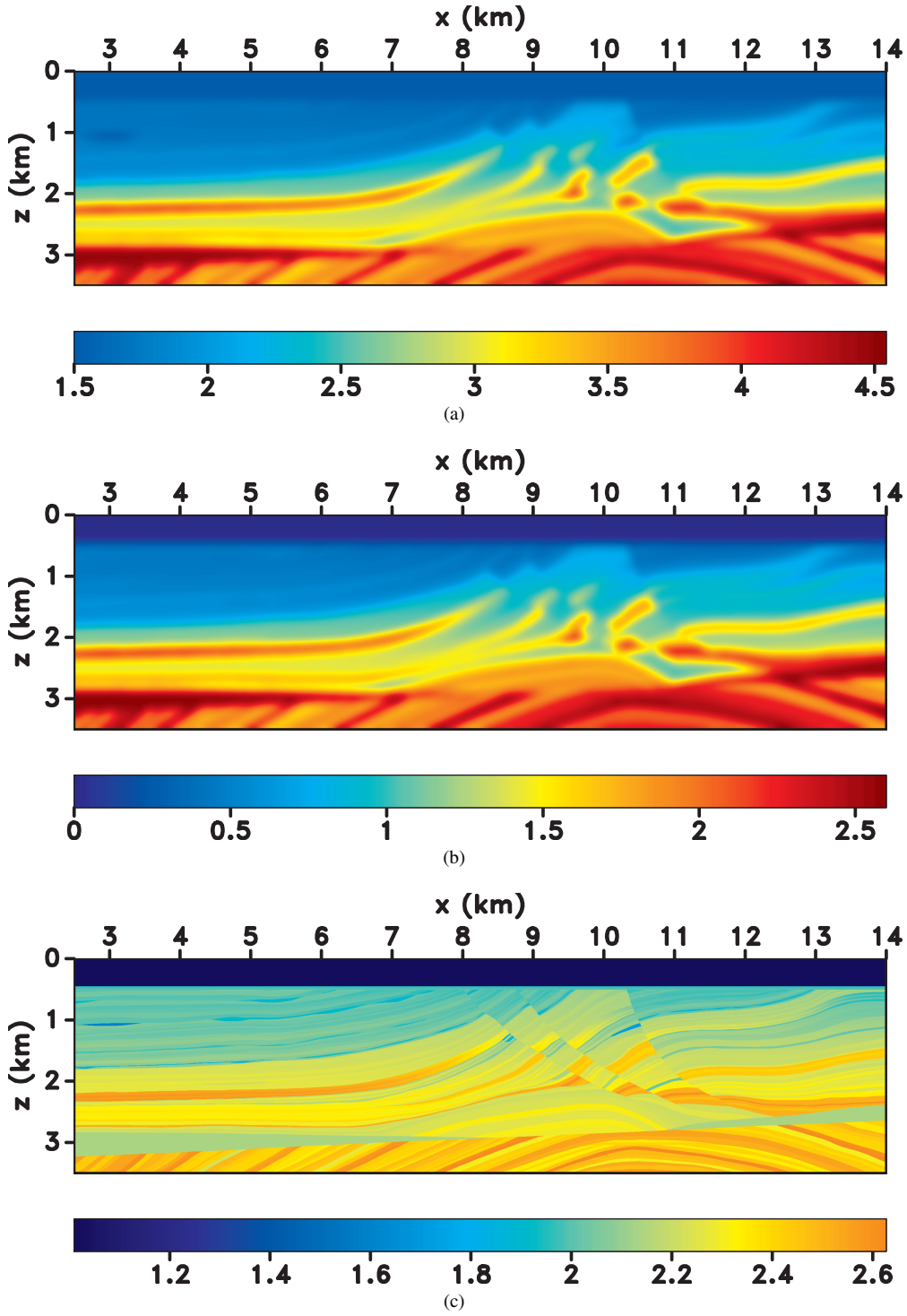

Figure 4. Migration model parameters used for the Marmousi II experiment. (a) P- and (b) S-wave velocity along the local symmetry axis (V_{P0} and V_{S0}, in km/s). (c) Stratigraphic density model used to generate synthetic data (in g/cm^3).

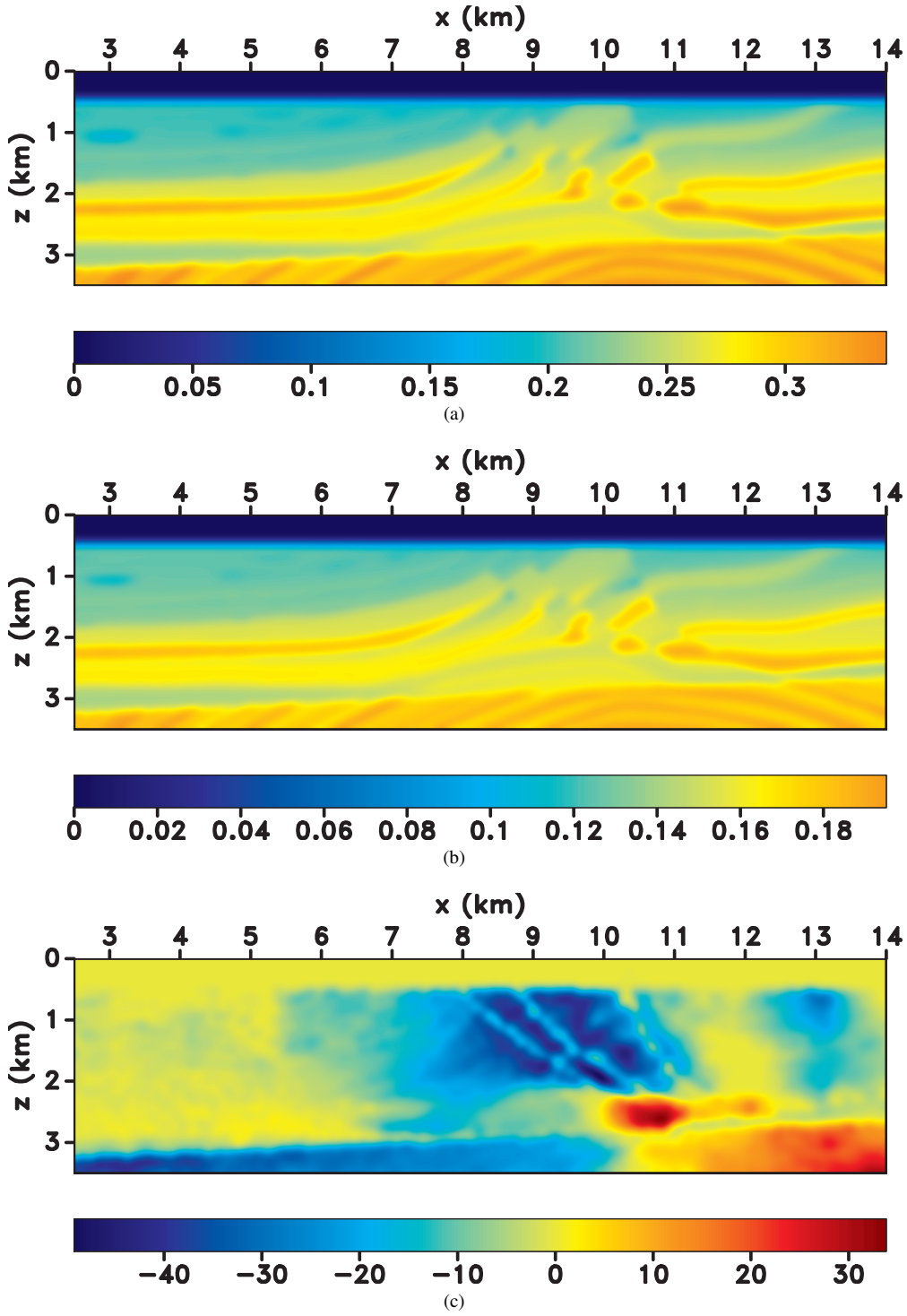

Figure 5. Migration anisotropy parameters used for the Marmousi II experiment. (a) ϵ, (b) δ, and (c) local tilt angle ν (in degrees).

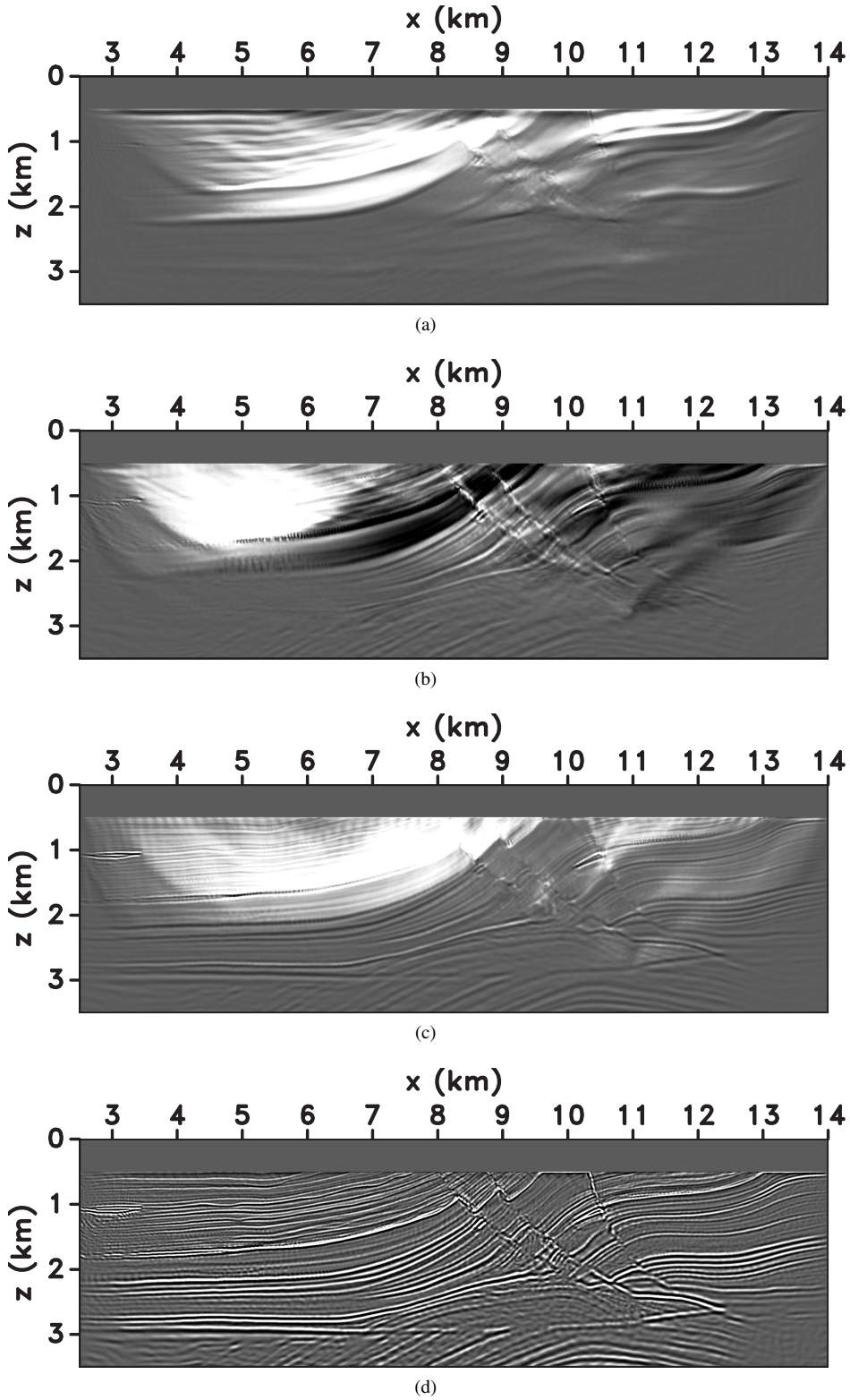

Figure 6. Images obtained from the Marmousi II experiment: conventional images using the correlation between displacement components (a) U_xV_x, (b) U_xV_z, and (c) U_zV_z; (d) energy image using the imaging condition in equation 35. Polarity reversal effects are visible in (b) by the change in polarity from the low-wavenumber artifacts. The energy image in (d) is the only one without low-wavenumber backscattering artifacts.

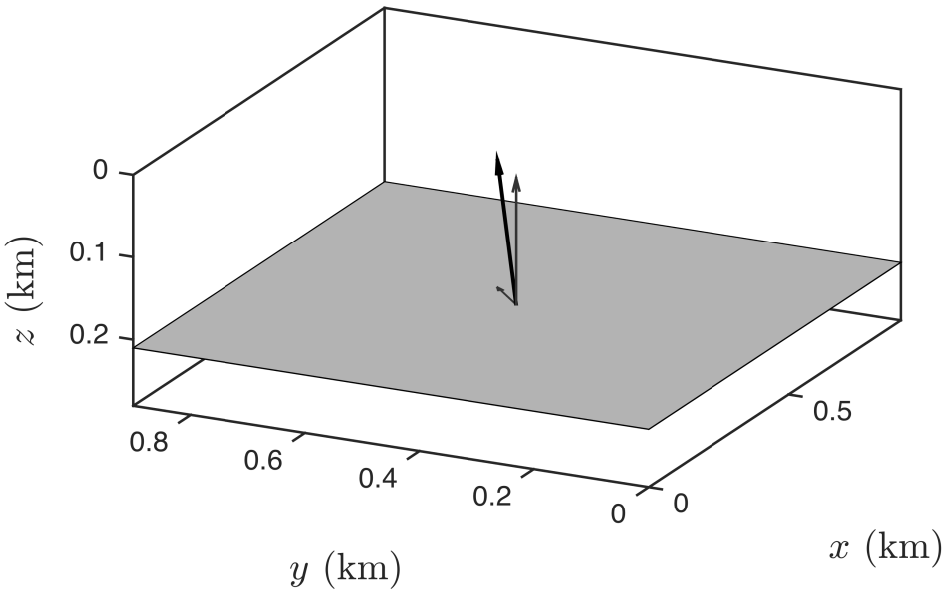

Figure 7. Schematic representation of the 3D TTI model used in the experiment of Figure 8. The black arrow indicates the tilted symmetry axis. The gray arrows indicate the projections of this vector onto the vertical axis and onto the reflection plane. Model parameters in the original system are $V_{P0} = 2.3$ km/s,$V_{S0} = 1.3$ km/s, $\rho = 2.0$ g/cm^3, $\epsilon = 0.4$, $\delta = 0.1$, and $\gamma = 0.0$.

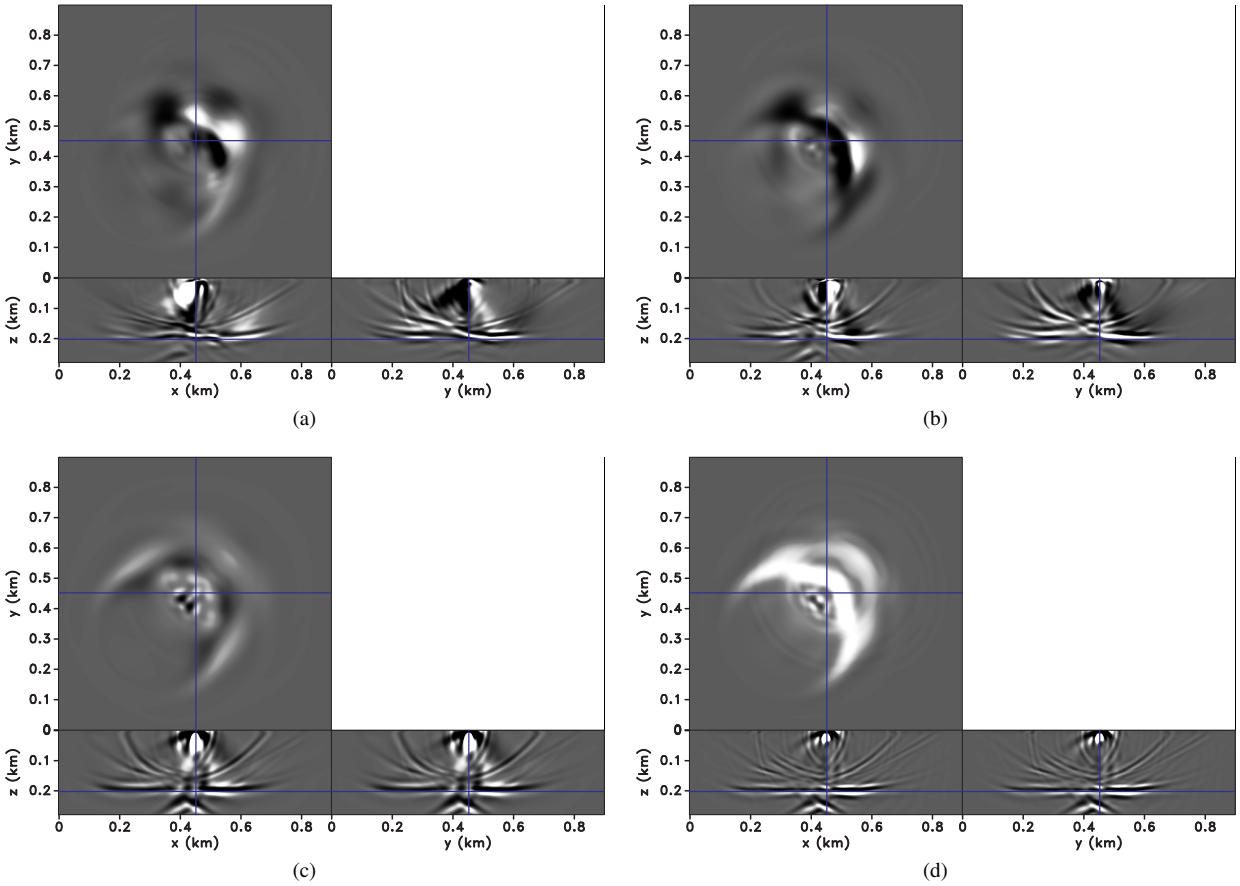

Figure 8. Images using the correlation between displacement components: (a) U_xV_y, (b) U_xV_z, and (c) U_zV_z; and an image using the energy imaging condition in (d). Artifacts due to the "fake" modes are present in all images. Backscattering artifacts and polarity reversal occur in the conventional images in (a)-(c) but not in the energy image in (d).